

## Microstructural analyses of aluminum–magnesium–silicon alloys welded by pulsed Nd:YAG laser welding

Hossain Ebrahimzadeh, Hassan Farhangi, Seyed Ali Asghar Akbari Mousavi, and Arman Ghahramani

Cite this article as:

Hossain Ebrahimzadeh, Hassan Farhangi, Seyed Ali Asghar Akbari Mousavi, and Arman Ghahramani, Microstructural analyses of aluminum–magnesium–silicon alloys welded by pulsed Nd: YAG laser welding, *Int. J. Miner. Metall. Mater.*, 27(2020), No. 5, pp. 660-668. <https://doi.org/10.1007/s12613-020-2027-y>

View the article online at [SpringerLink](#) or [IJMMM Webpage](#).

### Articles you may be interested in

A. R. Sufizadeh and S. A. A. Akbari Mousavi, [Microstructures and mechanical properties of dissimilar Nd:YAG laser weldments of AISI4340 and AISI316L steels](#), *Int. J. Miner. Metall. Mater.*, 24(2017), No. 5, pp. 538-549. <https://doi.org/10.1007/s12613-017-1435-0>

Zhen-hua Wang, Jian-jun Qi, and Wan-tang Fu, [Effects of initial grain size and strain on grain boundary engineering of high-nitrogen CrMn austenitic stainless steel](#), *Int. J. Miner. Metall. Mater.*, 25(2018), No. 8, pp. 922-929. <https://doi.org/10.1007/s12613-018-1641-4>

Dong-tao Wang, Hai-tao Zhang, Lei Li, Hai-lin Wu, Ke Qin, and Jian-zhong Cui, [The evolution of microstructure and mechanical properties during high-speed direct-chill casting in different Al-Mg<sub>2</sub>Si \*in situ\* composites](#), *Int. J. Miner. Metall. Mater.*, 25(2018), No. 9, pp. 1080-1089. <https://doi.org/10.1007/s12613-018-1659-7>

Slaana Laketi, Marko Rakin, Miloš Momilovi, Jovan Ciganovi, ore Veljovi, and Ivana Cvijovi-Alagi, [Surface modifications of biometallic CP-Ti and Ti-13Nb-13Zr alloy by picosecond Nd:YAG laser](#), *Int. J. Miner. Metall. Mater.*, In press. <https://doi.org/10.1007/s12613-020-2061-9>

Yong-sheng Sun, Yue-xin Han, Yan-feng Li, and Yan-jun Li, [Formation and characterization of metallic iron grains in coal-based reduction of oolitic iron ore](#), *Int. J. Miner. Metall. Mater.*, 24(2017), No. 2, pp. 123-129. <https://doi.org/10.1007/s12613-017-1386-5>



IJMMM WeChat



QQ author group

# Microstructural analyses of aluminum–magnesium–silicon alloys welded by pulsed Nd: YAG laser welding

Hossain Ebrahimzadeh, Hassan Farhangi, Seyed Ali Asghar Akbari Mousavi, and Arman Ghahramani

School of Metallurgy and Materials Engineering, College of Engineering, University of Tehran, Tehran 11155-4563, Iran  
(Received: 26 October 2019; revised: 20 January 2020; accepted: 21 January 2020)

**Abstract:** Revealing grains and very fine dendrites in a solidified weld metal of aluminum–magnesium–silicon alloys is difficult and thus, there is no evidence to validate the micro- and meso-scale physical models for hot cracks. In this research, the effect of preheating on the microstructure and hot crack creation in the pulsed laser welding of AA 6061 was investigated by an optical microscope and field emission electron microscopy. Etching was carried out in the gas phase using fresh Keller’s reagent for 600 s. The results showed that the grain size of the weld metal was proportional to the grain size of the base metal and was independent of the preheating temperature. Hot cracks passed the grain boundaries of the weld and the base metal. Lower solidification rates in the preheated samples led to coarser arm spacing; therefore, a lower cooling rate. Despite the results predicted by the micro and meso-scale models, lower cooling rates resulted in increased hot cracks. The cracks could grow in the weld metal after solidification; therefore, hot cracks were larger than predicted by the hot crack prediction models.

**Keywords:** etching technique; laser welding; inter-dendritic spacing; grain size; aluminum–magnesium–silicon alloys; hot crack formation model

## 1. Introduction

The aluminum–magnesium–silicon alloys have special industrial applications, such as in the building of planes, trucks, towers, yachts, and other structures. This is due to their outstanding corrosion resistance and suitable mechanical properties [1–2]. Fusion welding of one such aluminum alloy, 6061, is susceptible to hot crack formation [3–5]. The creation of hot cracks decreases weldability; therefore, many studies have investigated the issue of hot cracks. The relationship between welding parameters and hot crack formation requires further study. For this purpose, some criteria have been developed for the prediction of hot crack initiation and propagation such as threshold stress, and strain, or strain rate [6–7]. Nonetheless, new micro- and meso-scale models of hot cracks are based on the solidification microstructure [8–11]. According to these new models, during solidification, molten metal needs to flow in the two-phase (solid + liquid) region to feed the dendrite roots. If the feeding is enough to compensate for the contraction caused by solidification, no hot crack is formed. Indeed, the balance between feeding and consumption of the molten metal determines the probability

of hot crack occurrence [12–14]. Solving these model equations showed that solidification rate, grain size, and inter-dendritic arm spacing are the important parameters that affect hot crack initiation and propagation [15–17]. Inability to observe very fine solidified dendrites in the weld microstructure causes difficulties in the microstructural investigation of the hot crack formation and the evaluation of available models that define the relationship between welding parameters and hot cracks [17–19]. Difficulties in etching aluminum alloys have led to the utilization of modern methodologies, including high-resolution electron backscatter diffraction (EBSD) [20]. However, even with such a modern tool, dendrites in solidified microstructures cannot be seen [21]. Moreover, the method has sometimes caused the replacement of the analysis of the weld grains with only a macrograph of the weld [22–24]. The most common etching method is to immerse polished 6XXX aluminum alloy series in Keller’s reagent for 15 s. In the present paper, a modified etching technique is proposed. Also, the relationship between weld microstructure and hot cracks will be examined by etching the solidified dendrites and grains; results will be compared with the existing models for hot cracks.

## 2. Experimental

An industrial aluminum–magnesium–silicon alloy sheet, AA 6061-T6 (0.8 mm in thickness), was used as the base metal. Laser welding was performed with an 80W, SW-1 pulsed Nd:YAG laser machine in a “bead on plate” manner. The chemical composition is presented in Table 1. Preheat-

ing was performed by a resistance element heater. The welding parameters are provided in Table 2.

**Table 1. The chemical composition of 6061 aluminum alloy**

|         | Al   | Mg   | Si   | Cu   | Zn   | Mn   | Cr   | Fe   | Ti   | Ni |
|---------|------|------|------|------|------|------|------|------|------|----|
| Balance | 0.91 | 0.69 | 0.22 | 0.06 | 0.05 | 0.16 | 0.43 | 0.05 | 0.01 |    |

**Table 2. The parameters of laser welding**

| Sample No. | Pulse energy / J | Focal spot diameter / mm | Frequency / Hz | Duration time / ms | Welding speed / (mm·s <sup>-1</sup> ) | Preheating temperature / °C |
|------------|------------------|--------------------------|----------------|--------------------|---------------------------------------|-----------------------------|
| 1          | 4.8              | 0.5                      | 4              | 6                  | 0.50                                  | —                           |
| 2          | 4.8              | 0.5                      | 4              | 6                  | 0.50                                  | 100                         |
| 3          | 4.8              | 0.5                      | 4              | 6                  | 0.50                                  | 200                         |

For the etching process, a small amount of Keller’s reagent (Table 3) was poured into a watch glass, and the polished surface of the sample was immersed in the etchant. Fig. 1 shows the method of placing the sample in the etchant as well as the bubbles near the surface. Because etching was performed in the gas phase, the surface quality was very important and as the surface became more mirror-like, the quality of the etching was so improved. To investigate the etching time, the samples remained in the solution for 15 s and 600 s. In cases where the surface was not etched sufficiently, the duration could surpass 600 s. The etchant was freshly prepared since it was not usable after 30 min of preparation. Two samples were etched in the non-fresh solution for 300 s and 600 s, respectively. It should be mentioned that for the top surface of the weld seam, if the shielding gas was applied well, no treatments and/or polishing stages would be required due to the cleanliness and high solidification rate in the pulsed laser welding process.

The microstructures were analyzed with an optical microscope and a field emission scanning electron microscope. Clemex Image Analysis software was used to measure the grain sizes and the interdendritic spacing. X-ray diffraction (XRD) analysis was used for the identification of secondary phases in the aluminum matrix. The X-ray was produced in the XRD device by a copper target.

## 3. Results and discussion

### 3.1. Investigation of the base metal microstructure

The effect of etching time on the microstructure of AA 6061-T6 is shown in Fig. 2. The grain boundaries did not become visible after a common etching duration (15 s). The microstructure included equiaxed aluminum grains with an average grain size of 12 μm. The secondary phase grains of Mg<sub>2</sub>Si (Fig. 3) were dispersed. When performing the etching process as described above, the bubbles were accumulated on the surface and caused aluminum grains to be corroded by the gas phase (Fig. 1). 30 min after the solution preparation, the bubbles did not form in the etchant and, therefore, the etchant performance was degraded. In this case, when the sample was placed in the solution for a long period, the sample surface was totally covered by corrosion cavities in which the secondary phase was located. The observations for the alloy in the present study showed that this secondary phase prevented the grain boundaries from being etched. These particles were easily corroded by the etchant solution and served as sacrificial anodes for the matrix grain boundary. Hence, the grain boundaries were not exposed to corrosion. Fig. 4 shows the etching by the non-fresh solution for different etching time.

### 3.2. Investigation of the laser weld microstructure

The microstructures of the weldment in the center and the edges of the weld bead are shown in Figs. 5(a) and 5(b). The dendrites in the weld bead edge were parallel with the work-piece surface while they were perpendicular to the work-

**Table 3. Composition of the Keller’s reagent**

| H <sub>2</sub> O | HNO <sub>3</sub> | HCl | HF  |
|------------------|------------------|-----|-----|
| 95               | 2.5              | 1.5 | 2.0 |

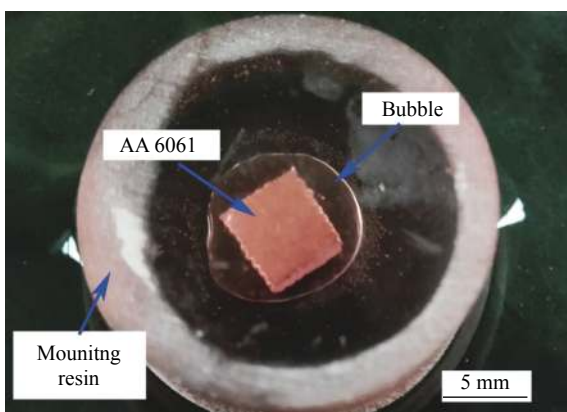


**Fig. 1. Immersion of the sample in the etchant. A bubble was created near the etching surface.**

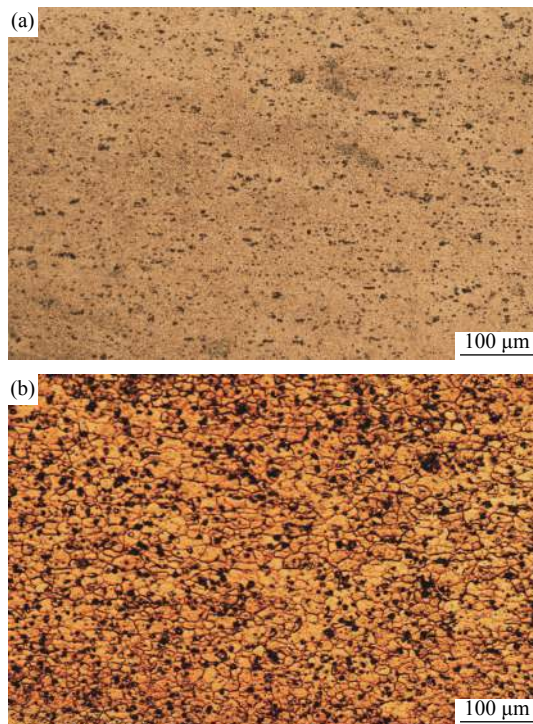


Fig. 2. The as-etched AA 6061-T6 in the fresh solution for different time: (a) 15 s; (b) 600 s.

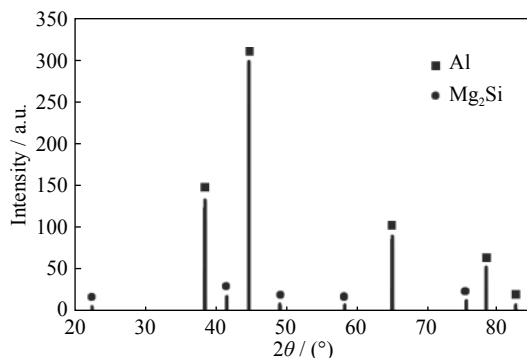


Fig. 3. X-ray diffraction pattern of AA 6061-T6 (showing aluminum and  $Mg_2Si$  peaks).

piece surface in the weld bead center. The reason for this is the start of solidification, which propagates from the edges of the weld pool to the weld bead center. As shown in the schematic in Fig. 5(c), the dendrites that had initiated from the bottom of the weld pool grew faster toward the weld bead center, and thus, they were perpendicular to the workpiece surface. As can be observed in Fig. 5(a), the start of solidification was planar in the weld pool edge followed by a dendritic form. Fig. 5(b) shows that cracks in the center of weld bead propagated between dendritic arms, thus they were associated with the final stage of solidification. A higher-magnification image of the dendrite microstructure is shown in Fig. 6. This figure shows the dimensions and the morphology of the dendrites. The growth of the dendrites occurred with no sec-

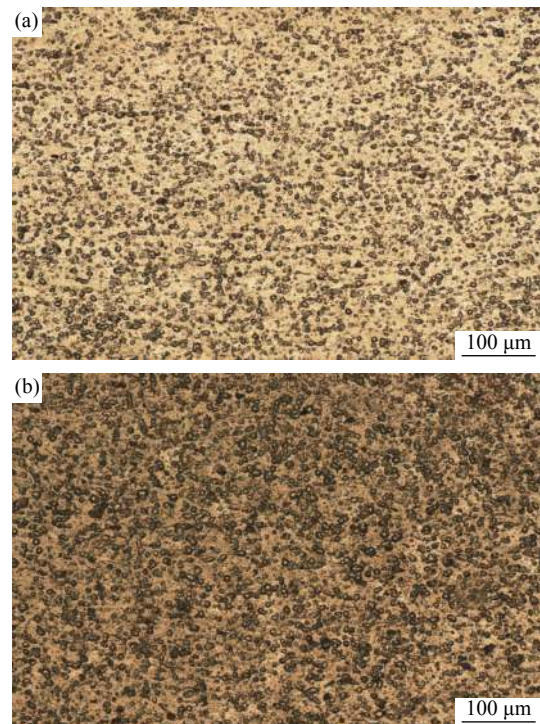


Fig. 4. The as-etched AA 6061 in the non-fresh solution for different time: (a) 300 s; (b) 600 s.

ondary arms.

The investigation of the weld cross-section (Fig. 7) revealed that the grain structure in the weld pool was affected by the base metal grains, i.e., the dendrite groups grew in the preferred direction of the base metal grains. Therefore, the difference in the orientation of the dendrite groups of each grain inside the weld metal was caused by the grain structure of the base metal. The parallel dendrites were placed in a weld grain and the dendrites in adjacent grains were in a different direction. The weld grains were columnar, their diameter was as large as the diameter of the base metal grains, and their height was dependent on the distance between two consecutive laser pulses. This is important because many studies [10,16] paid attention to the relationship between hot cracks and grain dimensions. They stated that the grain size refinement resulted in more difficult melt feeding, therefore, the probability of the formation of hot cracks increased. As will be mentioned in the following sections, despite the uniformity of the grain size in the samples as examined, the number of hot cracks was different. The dendrite arm spacings were 0.80, 1.03, 1.13  $\mu m$  for samples Nos. 1, 2, and 3, respectively. Increasing the preheating temperature led to an increase in the dendrite size. The non-preheated sample (No. 1) exhibited the finest microstructure. The hot cracks were formed along the grain boundaries in the weld metal and did not pass through the grains. These cracks continued inside the base metal and the partially melted zone.

The SEM images of the upper surface of the samples are

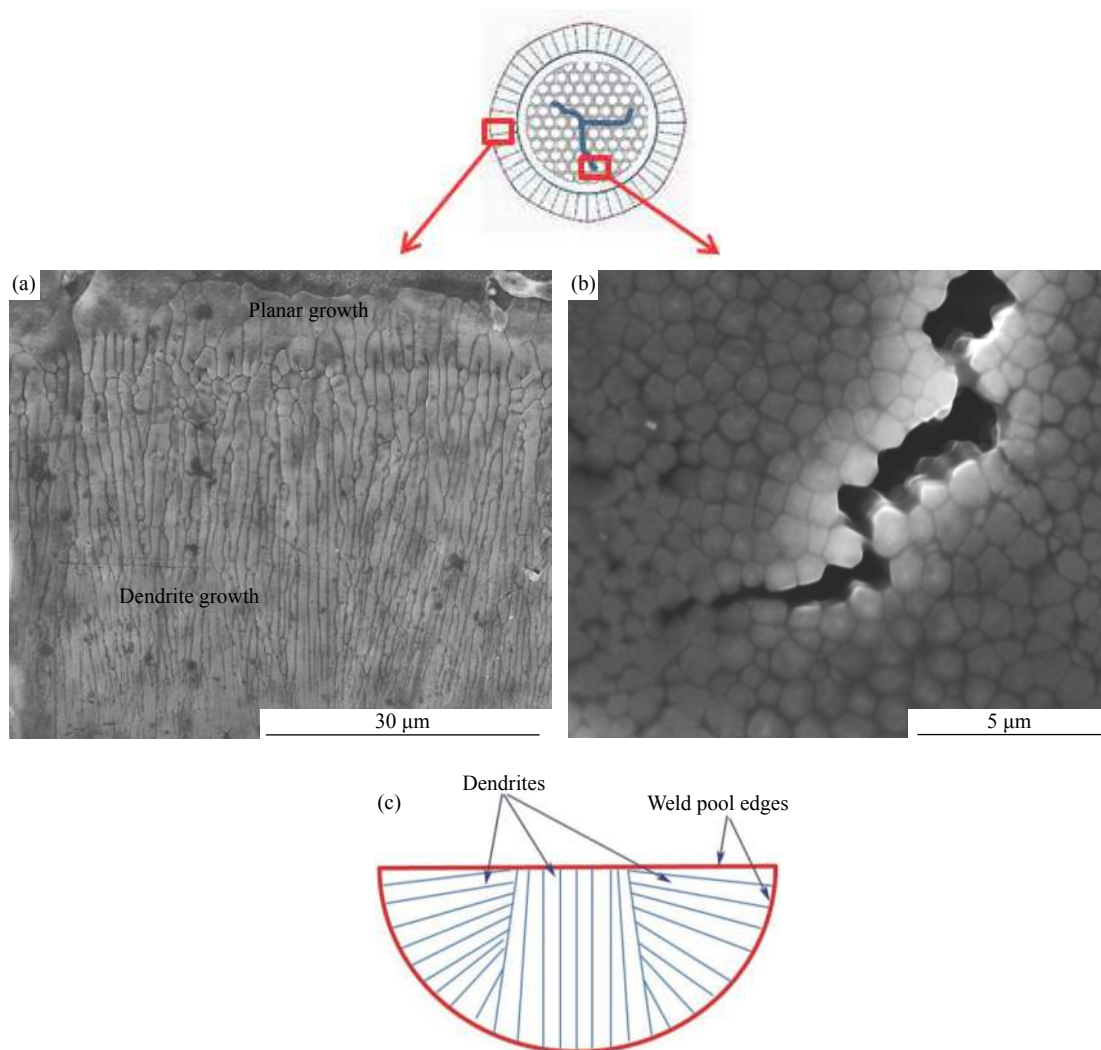


Fig. 5. The top view of the microstructure of the edge (a) and center of the single pulse weld bead (b); and the schematic of the growth of the dendrites (c).

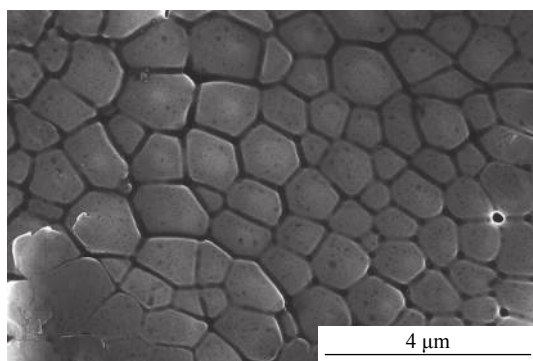
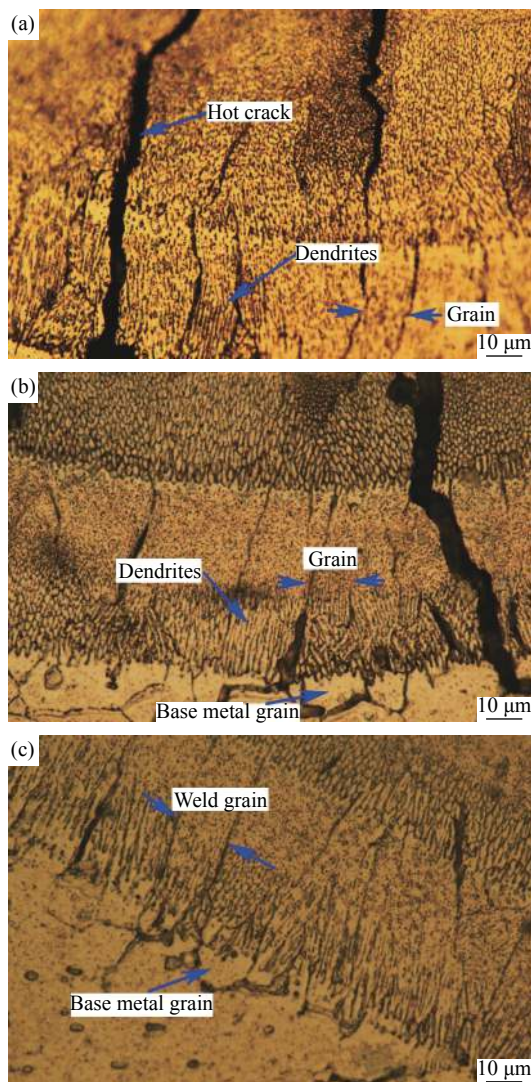


Fig. 6. Top-view SEM image of the solidified dendrites.

shown in Fig. 8. For the non-preheated sample, there were no regions of planar growth and the dendrites did not grow in long columns. Compared with the non-preheated sample, the growth mode at the first stage of solidification was planar and then converted to dendritic. The dendrites became thinner as

the solidification interface progressed.

To explain the difference between solidification morphologies, it is necessary to illustrate the relationship between the interface thermal gradient ( $G$ ) and solidification rate ( $R$ ), solidification interface morphology, and the effect of a preheating temperature on them. The interface type was determined as follows according to the relationship between  $G/R$  and  $\frac{\Delta T}{D_L}$ , where  $\Delta T$  is the solidification range in the phase diagram, and  $D_L$  is the diffusion coefficient in the liquid phase. If  $G/R > \frac{\Delta T}{D_L}$ , the interface will be planar, i.e., no undercooling forms in the solidification front. If  $G/R < \frac{\Delta T}{D_L}$ , due to the formation of undercooling, the melt/solid planar interface disappears and solid tabs inside the melt are formed. Considering the lower ratio of  $G/R$ , cellular, columnar, and equiaxed dendritic interfaces are created. In other words, at bigger  $G/R$ , there is a planar growth mode, and at smaller  $G/R$ , equiaxed dendritic growth is observed. Cooling rate ( $G \times R$ ) determines the microstructure size. Increasing the cooling rate results in finer



**Fig. 7.** The cross sections: (a) Sample No. 1; (b) Sample No. 2; (c) Sample No. 3.

microstructures as well as decreasing the dendrite arm spacing ( $\lambda$ ) [25]. The temperature gradient, which is discussed in solidification, progresses from the melt/solid interface toward the center of the weld pool (Fig. 9) [26]. It is well-known that the temperature of the solidification front has the same temperature as the aluminum melting point, and at the start of solidification the temperature of the center of the weld pool depends on heat source parameters such as energy amount and energy focus. Therefore, the thermal gradient did not undergo severe changes by preheating. Solidification is an exothermic process and it needs to dissipate the heat from the solid/liquid interface. In the preheated samples, the heat transfer decreased because of the lower temperature gradient in the base metal. In addition, in some research, it has been mentioned that, in the preheated samples, the solidification rate decreased [17]. Although some researchers [18] reported that preheating increased cooling rate, the appearance of

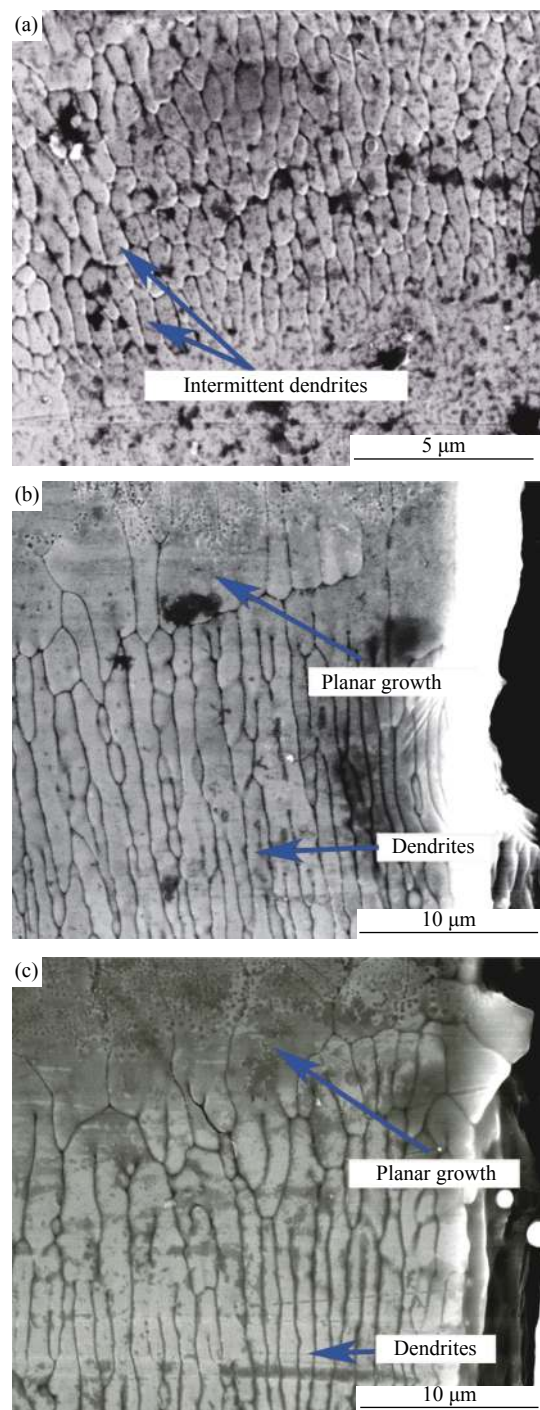


**Fig. 8.** The top-surface SEM images of the weld seam: (a) Sample No. 1; (b) Sample No. 2; (c) Sample No. 3.

dendrites and observation of coarser dendrites at higher preheating temperatures showed that the cooling rate had decreased. The reduction in the solidification rate due to increased preheating temperature, and the relative independence of the temperature gradient from the preheating temperature, caused solidification to start in a planar mode and to continue in a cellular mode in the preheated samples. Mean-

while, in the non-preheated sample, the high solidification rate produced finer intermittent dendrites. Planar growth in the preheated samples showed that increasing the preheating temperature resulted in a higher  $G/R$  ratio [25]. In a recent study, Hekmatjou and Naffakh-Moosavy [27] concluded that preheating led to a lower  $G/R$  ratio based on certain equations. However, in this study, the microstructural evidence showed that preheating increased the  $G/R$  ratio.

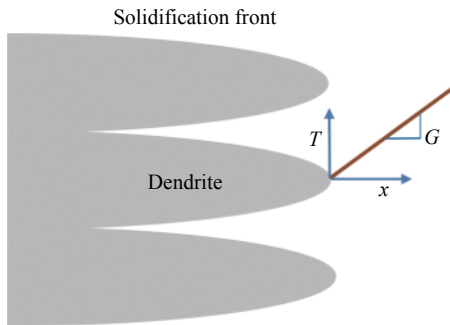


Fig. 9. Schematic illustration of the temperature gradient in the solidification front.

Fig. 10 displays the weld bead surface in a single pulse. The pattern of hot cracks was similar to that of the grain structure in the weld metal. Fig. 11 shows the top surface of sample No. 3. Here, the differences between the directions of dendrites on the crack edges could be seen. Also, the cross-sectional images of the laser-welded samples (Fig. 7) show very well that the weld cracks passed the adjacent grains rather than the adjacent dendrites. In the micro-scale models of hot cracks [13,17] (such as the Rappaz-Drezet-Gremaud [RDG] criteria), the equilibrium equations of melt feeding balance and its consumption were written for the interdendritic spaces but as can be seen from the images, the cracks were formed at the inter-grain spaces and the dendrites on both sides exhibited different orientations.

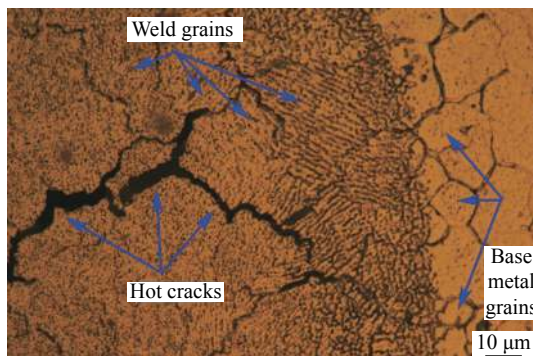


Fig. 10. The top view of weld bead surface welded by a single pulse laser (The dendrite orientation of grains can be seen).

Fig. 12 shows the optical microscopy images of the laser welds with and without preheating. All the welding parameters of these samples were the same but continuous end-to-end

cracks could be seen in the preheated samples as well as some intermittent cracks in the non-preheated sample. Increasing the preheating temperature led to an increase in hot cracks.

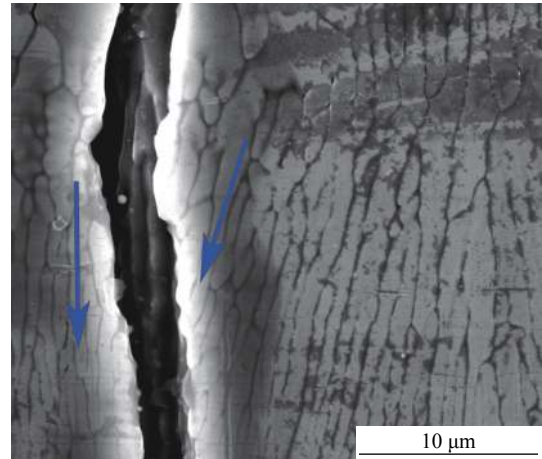
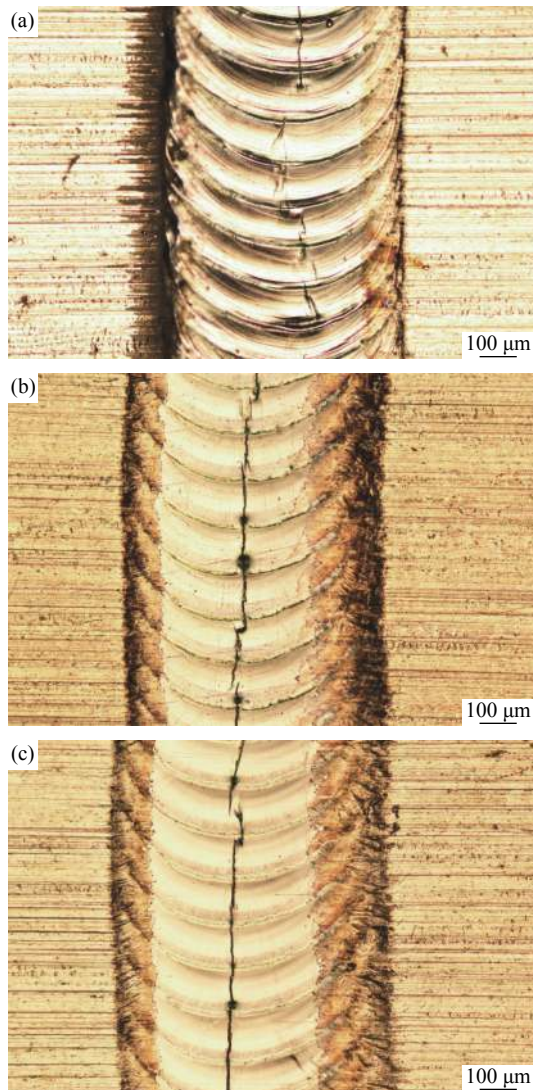


Fig. 11. The top surface of the laser-welded AA 6061-T6 preheated at 200°C.

The above-mentioned results have some contradictions with previous models for the prediction of hot cracks. The parameters that control the hot crack formation in these models are strain rate, solidification rate, the path spacing for the molten metal feeding, and the dendrite arm size. The length of the two-phase solid + melt region (the vulnerable zone) in the solidification frontline was an important parameter that affected molten metal feeding. Increasing the length of the two-phase solid + melt region increased the sensitivity to hot crack formation because the melt had to move longer distances to reach the roots of the dendrite, and the two-phase region acted as a barrier. The hot crack prediction models assume that the molten metal needs to pass through dendrite arms for feeding. But as mentioned above, the cracks were intergranular rather than interdendritic. The molten metal flow for feeding the hot crack nuclei was different along the grain boundaries compared with the interdendritic spaces. As previously mentioned, in the preheated samples,  $G/R$  was less than that in the non-preheated samples. Therefore, the two-phase region was of a reduced length (Fig. 8). However, the observations showed that reducing the two-phase solid + melt region did not reduce the total length of the hot cracks. On the other hand, according to the hot crack models, an increase in strain rate increases the possibility of generating hot cracks. The following equation shows the approximate strain rate:

$$\dot{\epsilon} = -\beta_T \dot{T}_{SL} = \beta_T |G \times R| \quad (1)$$

where  $\beta_T$  is the thermal contraction coefficient resulting from solidification and lower heat, and  $\dot{T}_{SL}$  is the cooling rate in the solid/melt interface. Consequently,  $\dot{\epsilon} \propto G \times R$ , therefore, any increase in  $\dot{\epsilon}$  increases the sensitivity to the hot cracks [19]. Despite the fact that the microstructure was coarser in



**Fig. 12.** The top view of the pulsed laser weld seams: (a) the non-preheated sample with a discontinued hot crack; (b) the sample preheated at 100°C with a continuous crack; (c) the sample preheated at 200°C with a continuous crack.

the preheated sample, which made  $G \times R$  and strain rate lower than those of the non-preheated sample, there were more hot cracks in the preheated samples. Previous studies [9,17] have shown that coarse dendrites and lower solidification rates decreased hot crack formation. The preheated samples have larger interdendritic spaces and lower solidification rate. However the total length of hot cracks increased. Revealing the dendrites proved that the aforementioned parameters were not the only effective parameters.

Figs. 13(a) and 13(b) show the final welding pulse performed at 100°C and 200°C, respectively. An increase in the preheating temperature led to a decrease in the length of the last-pulse hot crack. It meant that, although the total length of hot cracks along the weld line increased, it was reduced in the last pulse. These two observations showed that increasing the

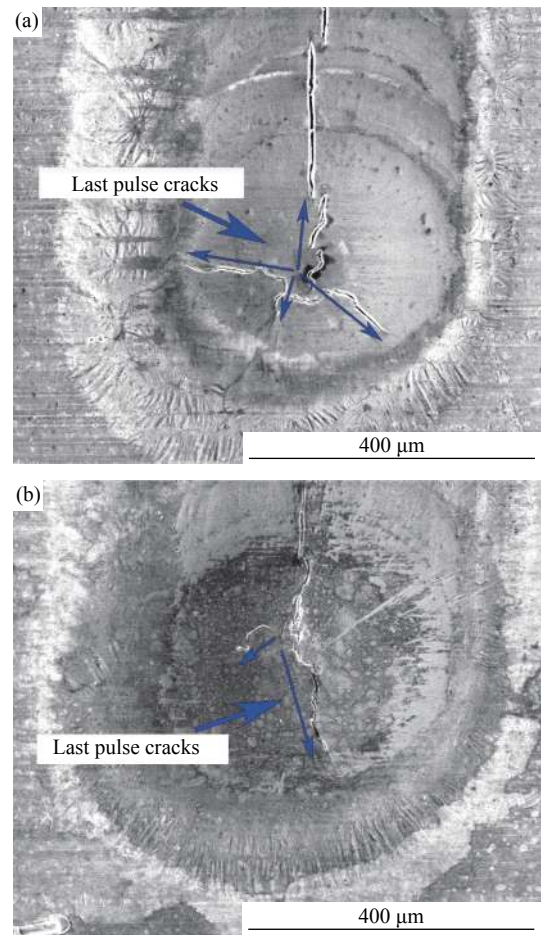


**Fig. 13.** The last pulse crack in the samples welded at 100°C (a) and 200°C (b).

preheating temperature reduced the amount of star cracks generated in each pulse, but increased the length of the longitudinal cracks. Fig. 14 shows the SEM images of the inside view of a crack. Different crack growth modes can be seen. The crack surface had some protrusions resulting from the fracture of the solidified material. It can be deduced that parts of the crack length were related to the regions that solidified previously but fractured by the stresses caused by welding. The final cracks that can be seen after the end of welding consisted of two hot and cold parts. That is, although an increase in the preheating temperature reduced the initial cracking, because the weld metal was cooled later and the grain boundaries reached enough strength over longer time, the stresses caused by the welding propagated the hot cracks and formed a final crack. In the non-preheated samples, the initial crack length was increased, but as the material reached sufficient strength during increased welding stress, cracks did not propagate in these samples. The larger cracks in the heat-affected zone of the preheated samples also confirmed this in another way: due to the higher temperature of the base metal and reduced strength, failure occurred more easily in the grain boundaries (Fig. 15). Therefore, any individual crack

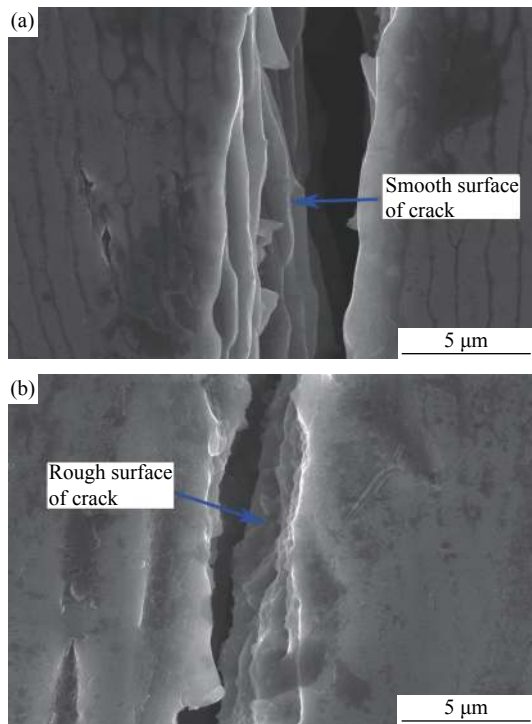


Fig. 14. The SEM images of an inside view of a crack in Sample 2: (a) smooth surface of crack; (b) rough surface of crack.

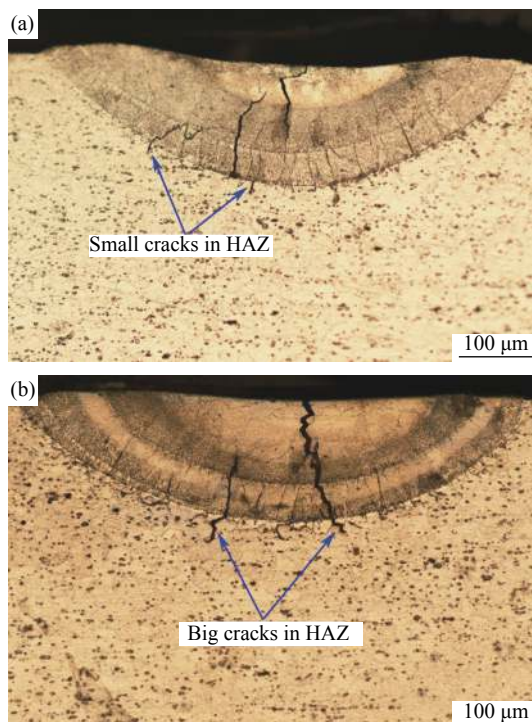


Fig. 15. The sample welded without preheating (a) and welded at the preheating temperature of 100°C (b).

that was created in each pulse of the pulsed welding followed the existing models for the formation of hot cracks. However, whenever a hot crack was observed on a welding

line that was formed by consecutive pulses, a disagreement with the prediction of the hot crack models occurred.

#### 4. Conclusions

(1) The grain size of the weld metal was not dependent on the preheating temperature, but was proportional to the grain size of the base metal. Hot cracks did not pass along parallel dendrites.

(2) Preheating in fusion welds decreased the cooling rate and resulted in a coarser structure. Despite the reduction in the solidification rate, and increasing the interdendritic spacing and relative stability of the temperature gradient, the length of hot cracks increased in the preheated samples.

(3) The propagation of hot cracks inside the solidified metal resulted in a disagreement between what was eventually observed as a hot crack and the micro- and meso-scale predictive models for the formation of hot cracks. Indeed, the existing models predict the length of a hot crack in a single pulse and for the total length of the weld; however, the fracture of newly solidified regions must be considered.

#### Acknowledgement

The authors would like to thank the metallography laboratory personnel of University of Tehran for their cooperation.

#### References

- [1] American Society for Metals, *ASM Handbook: Properties and Selection Nonferrous Alloys and Special Purpose Materials*, ASM International, USA, 1990, p. 401.
- [2] Y.M. Zhang, C. Pan, and A.T. Male, Improved microstructure and properties of 6061 aluminum alloy weldments using a double-sided arc welding process, *Metall. Mater. Trans. A*, 31(2000), No. 10, p. 2537.
- [3] American Society for Metals, *ASM Handbook, Welding Brazing and Soldering*, ASM International, USA, 1992, p. 1395.
- [4] T. Soysal and S. Kou, A simple test for assessing solidification cracking susceptibility and checking validity of susceptibility prediction, *Acta Mater.*, 143(2018), p. 181.
- [5] R.R. Ambriz, G. Mesmacque, A. Ruiz, A. Amrouche, and V.H. López, Effect of the welding profile generated by the modified indirect electric arc technique on the fatigue behavior of 6061-T6 aluminum alloy, *Mater. Sci. Eng. A*, 527(2010), No. 7-8, p. 2057.
- [6] L. Katgerman and D.G. Eskin, In search of the prediction of hot cracking in aluminium alloys, [in] T. Böllinghaus, H. Herold, C.E. Cross, and J.C. Lippold, eds., *Hot Cracking Phenomena in Welds II*, Springer, Berlin, Heidelberg, 2008, p. 11.
- [7] M. Wolf, T. Kannengießer, and T. Böllinghaus, Determination of critical strain rate for solidification cracking by numerical simulation, [in] T. Böllinghaus, H. Herold, C.E. Cross, and J.C. Lippold, eds., *Hot Cracking Phenomena in Welds II*, Springer, Berlin, Heidelberg, 2008, p. 77.
- [8] A. Niel, C. Bordreuil, F. Deschaux-Beaume, and G. Fras, Modelling hot cracking in 6061 aluminium alloy weld metal with

- microstructure based criterion, *Sci. Technol. Weld. Joining*, 18(2013), No. 2, p. 154.
- [9] S. Kou, A criterion for cracking during solidification, *Acta Mater.*, 88(2015), p. 366.
- [10] H.R.Z. Rajani and A.B. Phillion, A mesoscale solidification simulation of fusion welding in aluminum–magnesium–silicon alloys, *Acta Mater.*, 77(2014), p. 162.
- [11] H.R.Z. Rajani and A.B. Phillion, 3-D multi-scale modeling of deformation within the weld mushy zone, *Mater. Des.*, 94(2016), p. 536.
- [12] D.G. Eskin and L. Katgerman, A quest for a new hot tearing criterion, *Metall. Mater. Trans. A*, 38(2007), No. 7, p. 1511.
- [13] M. Rappaz, J.M. Drezet, and M. Gremaud, A new hot-tearing criterion, *Metall. Mater. Trans. A*, 30(1999), No. 2, p. 449.
- [14] N. Coniglio and C.E. Cross, Mechanisms for solidification crack initiation and growth in aluminum welding, *Metall. Mater. Trans. A*, 40(2009), No. 11, p. 2718.
- [15] C.E. Cross, N. Coniglio, P. Schempp, and M. Mousavi, Critical conditions for weld solidification crack growth, [in] T. Böllinghaus, J.C. Lippold, and C.E. Cross eds., *In Hot cracking phenomena in welds III*, Springer, 2011, p. 25.
- [16] H.R.Z. Rajani and A.B. Phillion, 3D multi-scale multi-physics modelling of hot cracking in welding, *Mater. Des.*, 144(2018), p. 45.
- [17] M. Sheikhi, F.M. Ghaini, and H. Assadi, Prediction of solidification cracking in pulsed laser welding of 2024 aluminum alloy, *Acta Mater.*, 82(2015), p. 491.
- [18] M. Sheikhi, F.M. Ghaini, and H. Assadi, Solidification crack initiation and propagation in pulsed laser welding of wrought heat treatable aluminium alloy, *Sci. Technol. Weld. Joining*, 19(2014), No. 3, p. 250.
- [19] P. von Witzendorff, S. Kaierle, O. Suttman, and L. Overmeyer, *In situ* observation of solidification conditions in pulsed laser welding of AL6082 aluminum alloys to evaluate their impact on hot cracking susceptibility, *Metall. Mater. Trans. A*, 46(2015), No. 4, p. 1678.
- [20] M.A. Abdulstaar, K.J. Al-Fadhlah, and L. Wagner, Microstructural variation through weld thickness and mechanical properties of peened friction stir welded 6061 aluminum alloy joints, *Mater. Charact.*, 126(2017), p. 64.
- [21] Q. Chu, R. Bai, H. Jian, Z. Lei, N. Hu, and C. Yan, Microstructure, texture and mechanical properties of 6061 aluminum laser beam welded joints, *Mater. Charact.*, 137(2018), p. 269.
- [22] S.D. Ji, X.C. Meng, Z.L. Liu, R.F. Huang, and Z.W. Li, Dissimilar friction stir welding of 6061 aluminum alloy and AZ31 magnesium alloy assisted with ultrasonic, *Mater. Lett.*, 201(2017), p. 173.
- [23] P. Sadeesh, M.V. Kannan, V. Rajkumar, P. Avinash, N. Arivazhagan, K.D. Ramkumar, and S. Narayanan, Studies on friction stir welding of AA 2024 and AA 6061 dissimilar metals, *Procedia Eng.*, 75(2014), p. 145.
- [24] A. Heidarzadeh, H. Khodaverdizadeh, A. Mahmoudi, and E. Nazari, Tensile behavior of friction stir welded AA 6061-T4 aluminum alloy joints, *Mater. Des.*, 37(2012), p. 166.
- [25] S. Kou, *Welding Metallurgy*, John Wiley & Sons, Inc., New Jersey, 2003, p. 199.
- [26] S. McFadden and D.J. Browne, A generalised version of an Ivantsov-based dendrite growth model incorporating a facility for solute measurement ahead of the tip, *Comput. Mater. Sci.*, 55(2012), p. 245.
- [27] H. Hekmatjou and H. Naffakh-Moosavy, Hot cracking in pulsed Nd: YAG laser welding of AA5456, *Opt. Laser Technol.*, 103(2018), p. 22.